Science Advances
AAAS

advances.sciencemag.org/cgi/content/full/6/25/eaba4935/DC1

Supplementary Materials for

Probing dynamical phase transitions with a superconducting quantum simulator

Kai Xu, Zheng-Hang Sun, Wuxin Liu, Yu-Ran Zhang, Hekang Li, Hang Dong, Wenhui Ren, Pengfei Zhang, Franco Nori, Dongning Zheng*, Heng Fan*, H. Wang*

*Corresponding author. Email: dzheng@iphy.ac.cn (D.Z.); hfan@iphy.ac.cn (H.F.); hhwang@zju.edu.cn (H.W.)

Published 17 June 2020, *Sci. Adv.* **6**, eaba4935 (2020)
DOI: 10.1126/sciadv.aba4935

This PDF file includes:

Device parameters. In Table S1, we present the characteristics of the quantum simulator with 16 out of the 20 qubits having XY-control lines. These 16 qubits are labelled in Fig. 1.

Correction of XY crosstalk. The characterization of the Z-crosstalk effect and its correction have been described in Ref. (*29*), which are also the same as in this experiment. In addition, the XY-drive crosstalks between qubits must be corrected, as all qubits are driven by identical microwave drives to quench the system. Different from the Z-crosstalk effects, the characterization of the XY-crosstalk effects includes the phase calibration of the microwave drives. Figure S1 shows the calibration process taking the measurement of the XY crosstalk effect of Q_2 to Q_1 as an example.

In Fig. S1a, to characterize the crosstalk amplitude, Q_1 is biased to the interacting frequency $\omega_I/2\pi$, while Q_2's frequency is tuned to a nearby one, e.g., ($\omega_I/2\pi$ – 0.08 GHz), and other qubits are decoupled from Q_1 and Q_2 by tuning their resonant frequencies far away. We apply a strong flat-top-envelope microwave pulse with frequency ω_I to Q_2's XY-control line, generating a crosstalk excitation on Q_1. We then monitor the evolution of Q_1's excitations for different resonant frequencies $(\omega_I - \delta_1)$ of Q_1 (δ_1 is a small deviation). By fitting the Rabi oscillation of the measured excited probabilities of Q_1, we can obtain the crosstalk amplitude of Q_2 to Q_1.

In Fig. S1b, we characterize the crosstalk phase of Q_2 to Q_1, with the same frequency arrangement as that in Fig. S1a. However, to cancel the crosstalk effect of Q_2 to Q_1, a microwave pulse on Q_1's XY-control line, with amplitude equal to the crosstalk amplitude of Q_2 to Q_1, should also be added. In this process, we monitor the evolution of Q_1's excitations for different phases of the microwave pulses on Q_2's XY-control line, while fixing the microwave phase of Q_1 to zero. The excitations of Q_1 are almost completely inhibited during the whole evolution process at a specific phase, as can be seen from Fig. S1b, showing that the phase difference of the microwave drives on the XY-control lines of Q_1 and Q_2 is π.

Calibrations of other pairs of qubits are performed with a similar method. After quantifying these crosstalk effects, we correct these issues in experiments by considering the case which only involves two qubits: Q_1 and Q_2. We bias these two qubits to $\omega_I/2\pi$ and simultaneously apply resonant microwave pulses on their XY-control lines with amplitudes $Ae^{i\phi_A}$ and $Be^{i\phi_B}$ for Q_1 and Q_2, respectively (other qubits are decoupled from Q_1 and Q_2 by tuning their resonant frequencies far away). Here ϕ_A and ϕ_B represent the microwave phases of Q_1 and Q_2, respectively. If no correction is made, the microwave amplitude and phase of each qubit can be represented as

$$\begin{bmatrix} Ae^{i\phi_A} + a_{12}Be^{i(\phi_{12}+\phi_B)} \\ a_{21}Be^{i(\phi_{21}+\phi_B)} + Be^{i\phi_B} \end{bmatrix} = \tilde{M}_{xy}^{Q_1,Q_2} \begin{bmatrix} Ae^{i\phi_A} \\ Be^{i\phi_B} \end{bmatrix},$$

where

$$\tilde{M}_{xy}^{Q_1,Q_2} = \begin{bmatrix} 1 & a_{12}e^{i\phi_{12}} \\ a_{21}e^{i\phi_{21}} & 1 \end{bmatrix}$$

is the XY-crosstalk matrix measured with the technique described above. On the contrary, if we set the microwave amplitudes and phases of the qubits to $A'e^{i\phi'_A}$ and $B'e^{i\phi'_B}$ in advance, the microwaves we apply to the XY-control lines should be corrected as

$$(\tilde{M}_{xy}^{Q_1,Q_2})^{-1} \begin{bmatrix} A'e^{i\phi'_A} \\ B'e^{i\phi'_B} \end{bmatrix}.$$

We have performed experiments to verify the validity of this XY-crosstalk correction, where we bias Q_1 and Q_2 to ω_I to open the interaction and simultaneously apply identical microwaves to these two qubits. The results are displayed in Fig. S2, demonstrating the validity of this correction. The same treatment can be easily extended to the multi-qubit case.

Note that in the experiments we apply two kinds of microwave drives on the qubits. One establishes the transverse field with the same driving frequency ω_I for all qubits, and the other is the rotation pulse applied at each qubit's idle frequency. The XY-crosstalk correction is only applied when we impose microwave drives on all the qubits, to generate identical transverse fields. As for the rotation pulses, the XY-crosstalk effects are negligible due to the large detuning between the idle points of qubits.

Calibration of the transverse field. The term of the local transverse field $h_j^x\sigma_j^x$ for each Q_j in Eq. (1) in the main text is enabled by the resonant microwave drives

	$\omega_j/2\pi$ (GHz)	$T_{1,j}$ (μs)	$T^*_{2,j}$ (μs)	$g_j/2\pi$ (MHz)	$\omega^r_j/2\pi$ (GHz)	$\omega^m_j/2\pi$ (GHz)	$F_{0,j}$	$F_{1,j}$
Q_1	4.835	33	1.7	27.6	6.768	4.815	0.979	0.928
Q_2	5.290	21	1.8	27.4	6.741	5.292	0.970	0.913
Q_3	5.330	37	1.8	29.1	6.707	5.350	0.978	0.920
Q_4	4.460	36	2.0	26.5	6.649	4.420	0.953	0.907
Q_5	4.791	32	2.8	29.2	6.611	4.792	0.980	0.893
Q_6	4.870	30	2.1	30.1	6.558	4.850	0.989	0.938
Q_7	4.569	25	2.2	24.1	6.551	4.450	0.980	0.933
Q_8	5.250	31	2.0	27.7	6.513	5.245	0.978	0.925
Q_9	4.680	23	2.4	27.3	6.524	4.765	0.967	0.926
Q_{10}	4.960	23	1.5	26.9	6.550	4.735	0.972	0.946
Q_{11}	4.899	32	1.6	29.1	6.568	4.880	0.985	0.924
Q_{12}	5.176	22	2.0	26.3	6.640	4.310	0.993	0.941
Q_{13}	5.220	34	2.0	26.5	6.659	5.205	0.987	0.942
Q_{14}	4.490	43	0.9	29.0	6.712	4.583	0.976	0.923
Q_{15}	4.415	>30	1.9	24.6	6.788	4.375	0.967	0.944
Q_{16}	4.766	37	1.5	27.5	6.758	4.906	0.970	0.945

TABLE S1. **Quantum simulator characteristics.** Here, ω_j is the idle frequency of Q_j, where single-qubit rotation pulses are applied. $T_{1,j}$ and $T^*_{2,j}$ are the energy relaxation time and Ramsey dephasing time (Gaussian decay) of Q_j, respectively, which are measured at the interacting frequency ω_I (= $\omega_{\mathcal{R}}$ + Δ); g_j denotes the coupling strength between Q_j and the resonator bus $\mathcal{R}$; ω^r_j is the resonant frequency of Q_j's readout resonator; ω^m_j is the resonant frequency of Q_j at the beginning of the measurement process, when its readout resonator is pumped with microwave pulses. Finally, $F_{0,j}$ ($F_{1,j}$) is the probability of detecting Q_j in the $|0\rangle$ ($|1\rangle$) state, when it is prepared in the $|0\rangle$ ($|1\rangle$) state.

with calibrated magnitude and phase. To ensure the uniformity of the driving magnitude, we perform Rabi oscillation measurements on each stand-alone qubit Q_j at the interacting frequency ω_I. The qubit exposed to the resonant microwave drive will experience an oscillation of its excited-state probability, where the oscillation frequency h^x_j/π can be adjusted by the driving amplitude. For the phase calibration of the transverse field, when applying microwave drives with a flat-top envelope to each Q_j, we actually obtain the form $h^x_j(e^{-i\phi_j}\sigma^+_j + e^{i\phi_j}\sigma^-_j)$, where ϕ_j is the microwave phase sensed by each Q_j and may be different from each other, because of the length disparities between each Q_j's XY-control wires. The experiments require the uniformity of ϕ_j, which can be achieved by the following calibration process. Here, we consider two qubits (Q_1 and Q_j), equally detuned from the resonator bus by $\Delta/2\pi \simeq -450$ MHz and driven by resonant microwaves through their own XY-control lines with the driving phases of these two qubits set to 0 and ϕ_j, respectively. The two-qubit Hamiltonian can be written as

$$\begin{aligned} H_{1j}/\hbar =& \lambda_{1j}(\sigma^-_1\sigma^+_j + \sigma^-_j\sigma^+_1) \\ &+ h^x(\sigma^x_1 + e^{-i\phi_j}\sigma^+_j + e^{i\phi_j}\sigma^-_j), \end{aligned}$$

where λ_{1j} is the coupling strength between Q_1 and Q_j, and h^x represents the driving magnitude on the two qubits. In experiments, we start with the ground state and monitor the evolution of the two-qubit system under the above Hamiltonian for different values of ϕ_j. We select Q_1 as the reference and adjust the ϕ_j of other qubits to make them pairwise aligned with that of Q_1. Note that when performing the phase check of Q_1 and Q_j at the interacting point ω_I, the frequencies of other qubits are arranged in the vicinity (about 50 to 100 MHz away from ω_I) to minimize the Z-crosstalk effect. The calibration sequence and experimental results for different ϕ_j are displayed in Fig. S3. We note that the calibration of the transverse field cannot ensure the ideal uniformity of the microwave drives. Thus, we numerically consider a small inhomogeneity in the phases of the microwave drives for the 16 qubits, and find that our numerical results show a better agreement with the experimental results if ϕ_j is drawn from a normal distribution with an average value 0 and a standard deviation 0.08.

Phase calibration of the rotation pulse. As can be seen from Fig. 1c, after the evolution under the quenched Hamiltonian, we apply the rotation pulse on each qubit before the joint readout to measure the physical quantities, including the average spin magnetizations $\langle\sigma^x(t)\rangle$ and $\langle\sigma^y(t)\rangle$. The rotation operation on each qubit is realized by a Gaussian-envelope microwave pulse with a full width at half maximum of 20 ns, which has been characterized by randomized benchmarking with a fidelity above 0.99 for both $X_{\pi/2}$ and $Y_{\pi/2}$ rotation gates.

To mainly compensate for the dynamic phase caused by frequency tuning through the sequence, the phase of each rotation pulse needs to be corrected. The calibration

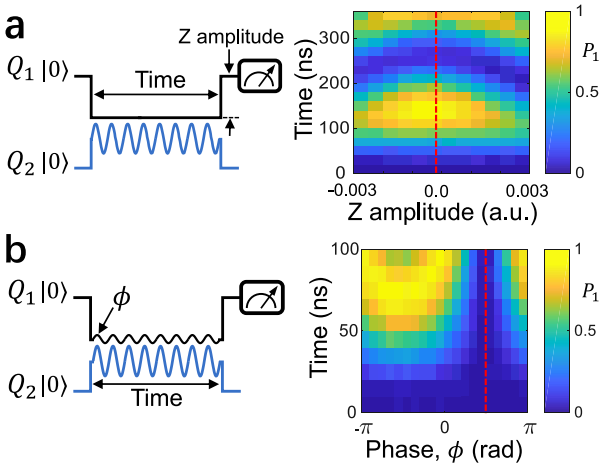

FIG. S1. **Quantification of XY-crosstalk effects. a**, Experimental sequence and results for measuring the XY-crosstalk amplitude. After tuning Q_1 to the interacting point ω_I, we apply a strong microwave drive ($h_2^x/2\pi \simeq$15 MHz) on Q_2's microwave drive line with resonant frequency ω_I. The strong drive will generate a crosstalk Rabi oscillation on Q_1. We measure the Rabi oscillations for different values of δ_1, among which the one with the slowest Rabi oscillation characterizes the crosstalk amplitude, as shown by the red vertical dashed line. **b**, Experimental sequence and results for the measurement of the XY-crosstalk phase. In our experiments, we add a microwave drive on Q_1's XY-control line with an adjustable phase ϕ. The selection of ϕ can induce an enhancement or neutralization effect (red dotted vertical line) on Q_1's Rabi oscillation, which can help us identify the XY-crosstalk phase.

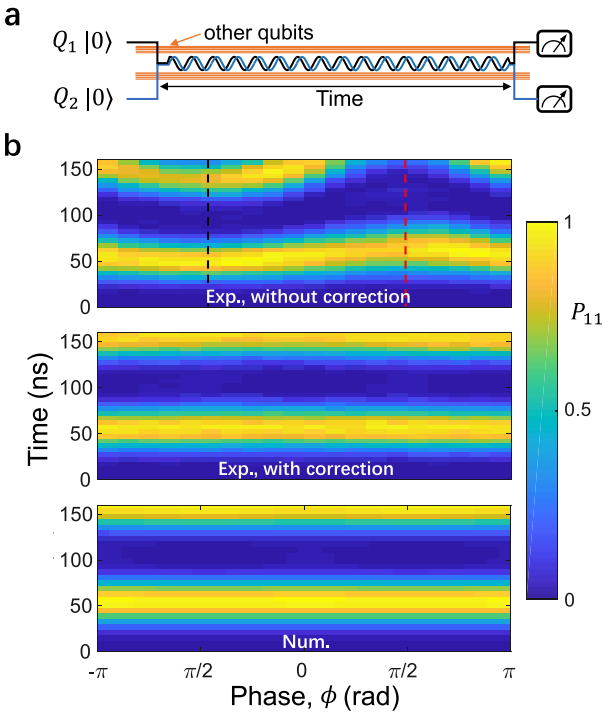

FIG. S2. **Experimental test of the XY-crosstalk correction. a**, The experimental sequence. We tune two qubits on resonance at ω_I, while other qubits are arranged in the vicinity, and apply resonant microwave drives ($h^x/2\pi \simeq$5 MHz for each qubit) on these two qubits' XY-control lines with a controllable phase difference of ϕ. **b**, The measured probabilities P_{11} of the $|11\rangle$-state, versus t and ϕ, in cases with and without applying the XY-crosstalk correction, compared with the numerical results. When no XY-crosstalk correction is made, the measured oscillation periods of P_{11} for different ϕ values show an obvious inconsistency, indicating an enhancement (black dotted vertical line) or neutralization (red dotted vertical line) effects induced by the XY crosstalk. After applying the XY-crosstalk correction, the experimental results are in good agreement with the numerical results.

process is presented in Fig. S3c, taking Q_1 as an example. The calibrated qubit is biased to the interacting frequency ω_I with a rectangular pulse, while the frequencies of other qubits are arranged in the vicinity, to minimize the Z-crosstalk effect. Almost simultaneously, Q_1 is driven by a flat-top-envelope microwave pulse with frequency ω_I. Then, we bias Q_1 back to its idle frequency and apply a $\pi/2$-rotation pulse before the readout. We record the probabilities of Q_1's excited state during this dynamics for different phases ϕ of the rotation pulse. The results are displayed in Fig. S3d, where the phase offset used for the correction is highlighted by the red dotted vertical line.

Numerical simulation on the effects of disordered couplings. As shown in Fig. 1B of the main text and Fig. S4a, although the experimental device can successfully simulate the LMG model, there still exists a disorder in the qubit-qubit couplings. To study the effects of the disordered couplings on the signatures of the DPT, we numerically study the Hamiltonian

$$H/\hbar = \sum_{i<j}^{16}(\lambda + \delta\lambda_{ij})(\sigma_i^+\sigma_j^- + \sigma_i^-\sigma_j^+) + h^x\sum_{j=1}^{16}\sigma_j^x, \quad \text{(S3)}$$

where λ is the mean value of the qubit-qubit couplings with $\lambda/2\pi \simeq 1.43$ MHz, and $\delta\lambda_{ij}$ follows a uniform distribution $[-W, W]$. The time-averaged magnetization $\overline{\langle\sigma^z\rangle}$ and the time-averaged correlation $\overline{C_{zz}}$ versus the transverse field with different disorder strengths W are depicted in Fig. S4b and S4c, respectively. The behaviors of $\overline{\langle\sigma^z\rangle}$ and $\overline{C_{zz}}$ of the ideal LMG model and our device are compared, which indicate that our device can be effectively described by Eq. (S3) using a disorder strength $W/2\pi \simeq 0.7$ MHz. Furthermore, we demonstrate that the

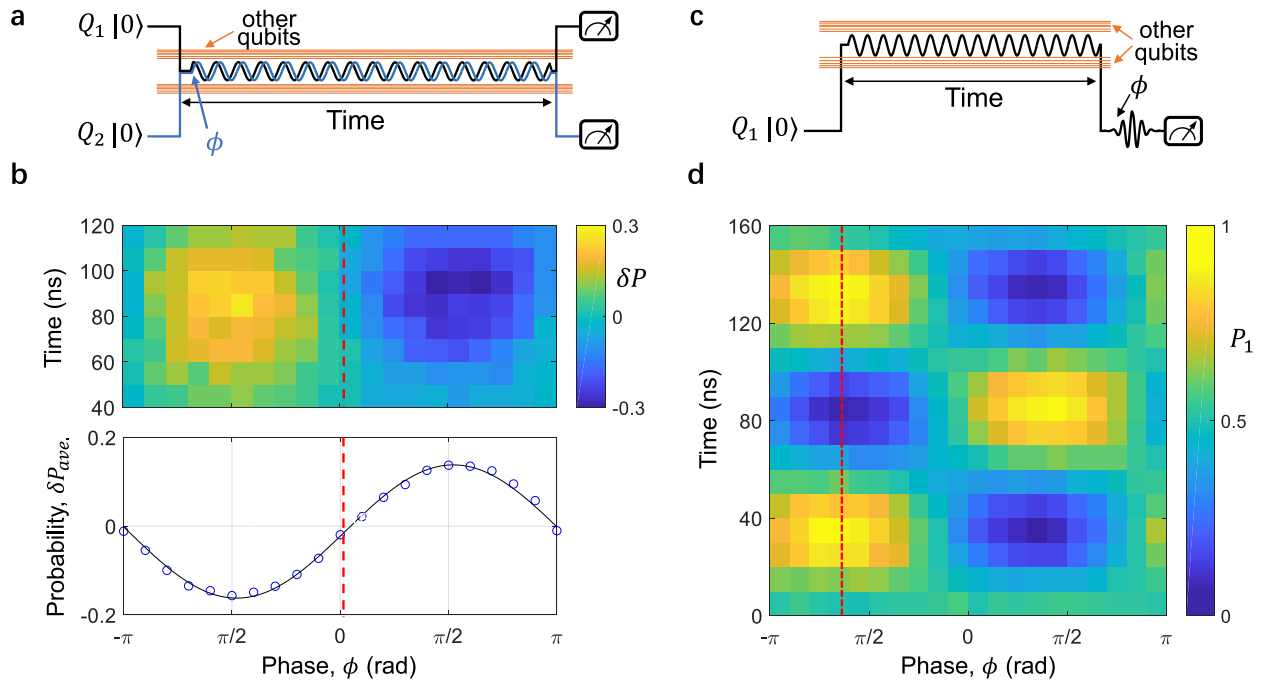

FIG. S3. **Phase alignment of the transverse field and the rotation pulse.** **a**, Experimental sequence. Two qubits (Q_1 and Q_2) are detuned from the resonator bus $\mathcal{R}$ by the same amount $\Delta/2\pi \simeq -450$ MHz, while other qubits are arranged in the vicinity of this point to minimize Z-crosstalk effects. We then apply resonant microwave drives on these two qubits with the same magnitude ($h^x/2\pi \simeq 2$ MHz) but a phase difference of ϕ and monitor the dynamics from 40 ns to 120 ns by recording the probabilities of Q_1 and Q_2, denoted as $P_1^{Q_1}$ and $P_1^{Q_2}$. **b**, 2D graph of $\delta P \equiv P_1^{Q_2} - P_1^{Q_1}$ as a function of t and ϕ (top) and the time-averaged δP (bottom). We fit this curve with a sine function to extract the phase offset (red dotted vertical line), which will be added to the microwave drive of Q_2 to ensure the phase alignment between these two qubits. **c**, Experimental sequence taking Q_1 as an example. The qubit Q_1 is detuned from the resonator bus $\mathcal{R}$ by about $\Delta/2\pi \simeq -450$ MHz, while other qubits are arranged in the vicinity of this point to minimize Z-crosstalk effects. Simultaneously, we apply on Q_1 resonant microwave drives with a magnitude of $h^x/2\pi \simeq 5$ MHz, after which we quickly bias Q_1 to its idle point and apply a rotation pulse with a specific phase ϕ before the readout. **d**, 2D graph of the measured excited probabilities P_1 as a function of t and ϕ. The phase offset pointed by the red dotted vertical line should be added to Q_1's rotation pulse to align the phases.

disordered qubit-qubit couplings do not drastically influence the signatures of the DPTs. In details, the finite and zero values of $\overline{\langle\sigma^z\rangle}$ in the DFP and DPP, respectively, as well as the local minimum of $\overline{C_{zz}}$ can all be observed in the ideal LMG model, our quantum simulator, and the Hamiltonian in Eq. (S3) with a relatively small strength of disorder $W/2\pi \leq 1$ MHz.

Measurement of the spin-squeezing parameter. The calculation of the spin-squeezing parameter ξ^2 consists of the following steps. The first step is to calculate the mean-spin direction $\vec{n}_0 = (\sin\theta\cos\phi, \sin\theta\sin\phi, \cos\theta)$, where

$$\theta = \arccos\left(\frac{\mathcal{S}^z}{|\vec{\mathcal{S}}|}\right),$$

and

$$\phi = \begin{cases} \arccos\left(\frac{\langle\mathcal{S}^x\rangle}{|\vec{\mathcal{S}}|}\right) & \text{if} \quad \langle\mathcal{S}^y\rangle > 0 \\ 2\pi - \arccos\left(\frac{\langle\mathcal{S}^x\rangle}{|\vec{\mathcal{S}}|}\right) & \text{if} \quad \langle\mathcal{S}^y\rangle < 0 \end{cases},$$

with $|\vec{\mathcal{S}}|^2 = \langle\mathcal{S}^x\rangle^2 + \langle\mathcal{S}^y\rangle^2 + \langle\mathcal{S}^z\rangle^2$. The second step is to obtain the expression of $\mathcal{S}_{\vec{n}_\perp}$ and to minimize its variance. We can obtain two orthogonal bases, $\vec{n}_1 = (-\sin\phi, \cos\phi, 0)$ and $\vec{n}_2 = (\cos\theta\cos\phi, \cos\theta\sin\phi, -\sin\theta)$, perpendicular to $\vec{n}_0$. Then, $\mathcal{S}_{\vec{n}_\perp}$ can be represented as $\vec{\mathcal{S}}\cdot\vec{n}_\perp$, with $\vec{n}_\perp = \vec{n}_1\cos\vartheta + \vec{n}_2\sin\vartheta$, and $\vartheta \in [0, 2\pi]$. The minimum in Eq. (2) of the main text is actually equivalent to the optimization of ϑ. It turns out that the optimum procedure

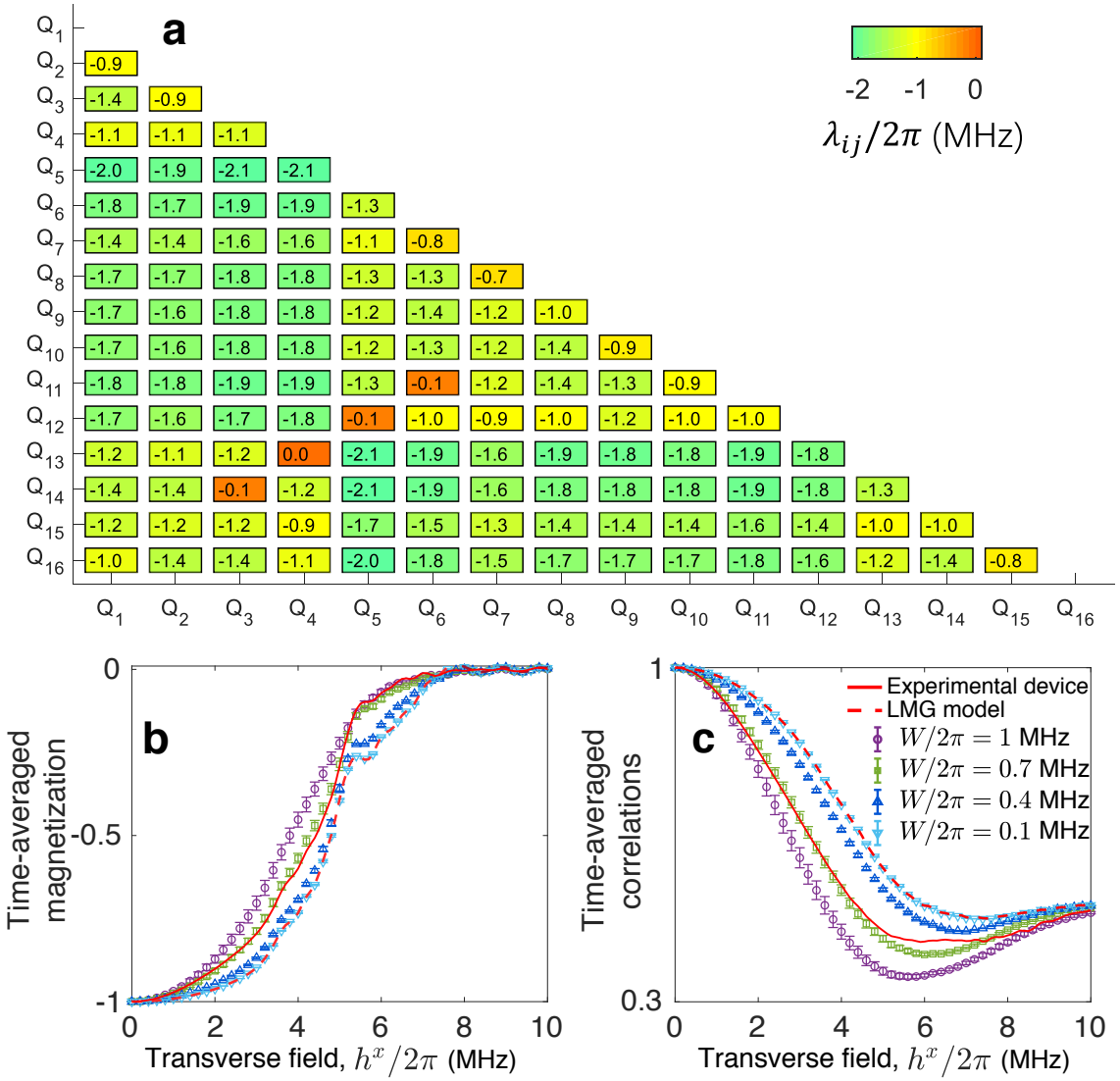

FIG. S4. **Coupling matrix and the effects of disordered couplings on the DPT. a**, The matrix presenting the qubit-qubit coupling strengths. **b**, The numerical results of the time-averaged magnetization $\overline{\langle\sigma^z\rangle}$ as a function of the transverse field for the LMG model, our quantum simulator with coupling strengths shown in **a**, and the Hamiltonian in Eq. (S3) with different disorder strengths W. **c** is similar to **b** but shows the results of the averaged spin correlation $\overline{C_{zz}}$.

finally gives an elegant formula

$$\xi^2 = \frac{2}{N}[\langle(\mathcal{S}^{\vec{n}_1})^2 + (\mathcal{S}^{\vec{n}_2})^2\rangle - \sqrt{\langle(\mathcal{S}^{\vec{n}_1})^2 - (\mathcal{S}^{\vec{n}_2})^2\rangle^2 + \langle\{\mathcal{S}^{\vec{n}_1}, \mathcal{S}^{\vec{n}_2}\}\rangle^2}], \quad \text{(S4)}$$

with $\{\mathcal{S}^{\vec{n}_1}, \mathcal{S}^{\vec{n}_2}\} = \mathcal{S}^{\vec{n}_1}\mathcal{S}^{\vec{n}_2} + \mathcal{S}^{\vec{n}_2}\mathcal{S}^{\vec{n}_1}$.

We measure $\langle(S^{\vec{n}_1})^2\rangle$ and $\langle(S^{\vec{n}_2})^2\rangle$ by applying single-qubit rotations to move the $\vec{n}_1$ ($\vec{n}_2$) axis in the Bloch sphere to the z-axis before readout. For $\langle\{\mathcal{S}^{\vec{n}_1}, \mathcal{S}^{\vec{n}_2}\}\rangle$, it boils down to the measurement of two-spin correlators

$$\langle\{\mathcal{S}^{\vec{n}_1}, \mathcal{S}^{\vec{n}_2}\}\rangle = \frac{1}{4}(\sum_{i\neq j}\langle\sigma_i^{\vec{n}_1}\sigma_j^{\vec{n}_2}\rangle + \sum_{i\neq j}\langle\sigma_i^{\vec{n}_2}\sigma_j^{\vec{n}_1}\rangle).$$

To characterize the two spin correlators for all combinations ($16 \times 15 \times 2$), we adopt the following methods: First, we divide the 16 qubits into 2 groups randomly, e.g., $G_1^1 = \{Q_1$–$Q_8\}$ and $G_2^1 = \{Q_9$–$Q_{16}\}$. Next, we apply rotation pulses on the qubits in G_1^1 to bring the $\vec{n}_1$-axis to the z-axis, and simultaneously apply other rotation pulses on qubits in G_2^1 to bring the $\vec{n}_2$-axis to the z-axis, after

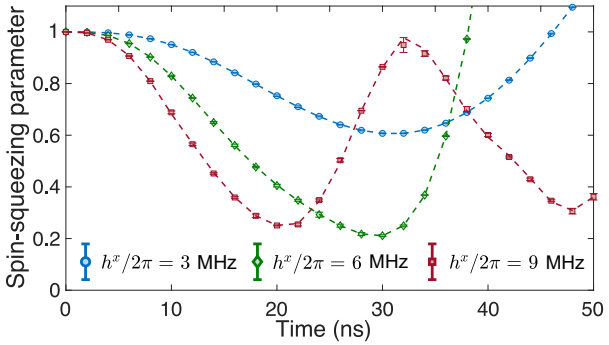

FIG. S5. **Numerical calculation of the dynamics of the spin-squeezing parameter.** The dashed curves are the strict results according to Eq. (S4), while the points are calculated with the method described above. To estimate the error bar, we repeat the calculation 5 times for different values of t and h^x. For each time, we randomly select 5 groups of $\{G_1^i, G_2^i\}$ and average the results.

which the 16-qubit joint readout is executed, yielding the probabilities P=$\{P_{00\ldots0}, P_{00\ldots1}, \ldots, P_{11\ldots1}\}$. Finally, by calculating $\sum_{j=1}^{2^{16}} P_j \mathcal{S}_{j,j}^{zz(G_1^1,G_2^1)}$, with $\mathcal{S}^{zz(G_1^1,G_2^1)}$ written as

$$\mathcal{S}^{zz(G_1^1,G_2^1)} = \sum_{i\epsilon G_1^1} \sigma_i^z \sum_{j\epsilon G_2^1} \sigma_j^z,$$

we obtain the summation of two-spin correlators for $8 \times 8 = 64$ combinations (Q_1–Q_9, Q_1–Q_{10}, ..., Q_1–Q_{16}, Q_2–Q_9, ..., Q_8–Q_{16}), i.e.,

$$P_{n_1n_2}^1(G_1^1, G_2^1) = \sum_{i\epsilon G_1^1, j\epsilon G_2^1} \langle \sigma_i^{\vec{n}_1} \sigma_j^{\vec{n}_2} \rangle.$$

Moreover, by exchanging the rotation pulses applied to qubits in these two groups, we can obtain

$$P_{n_2n_1}^1(G_1^1, G_2^1) = \sum_{i\epsilon G_1^1, j\epsilon G_2^1} \langle \sigma_i^{\vec{n}_2} \sigma_j^{\vec{n}_1} \rangle.$$

After repeating this process 5 times, where 16 qubits are divided into two different groups of equal size, we can approach $\langle \{\mathcal{S}^{\vec{n}_1}, \mathcal{S}^{\vec{n}_2}\} \rangle$ by averaging the overall results

$$\frac{16 \times 15}{64 \times 5} \sum_{i=1}^{5} [P_{n_1n_2}^i(G_1^i, G_2^i) + P_{n_2n_1}^i(G_1^i, G_2^i)].$$

This method has been verified by numerical simulations that possess a very high precision, as illustrated in Fig. S5.

Finite-size effect of the Loschmidt echo in the LMG model. The results in the main text are in good agreement with the theoretical predictions based on the LMG

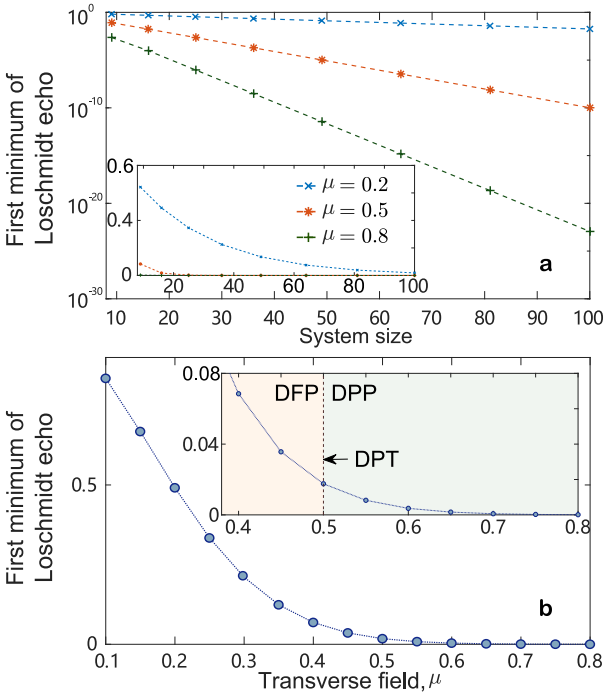

FIG. S6. **Numerical results of the Loschmidt echo in the LMG model.** **a**, The value of the first minimum of the Loschmidt echo $\mathcal{L}_{\text{min}}^{(1)}$ scales with the system's size N. **b**, The value of $\mathcal{L}_{\text{min}}^{(1)}$ as a function of g for $N = 16$.

model. It has been shown that the Loschmidt echo cannot be strictly equal to 0 in a finite-size LMG model (*28*). In Fig. S6a, we present the first minimum value of the Loschmidt echo $\mathcal{L}_{\text{min}}^{(1)}$ as a function of the LMG model's size N with $J = 1$ and different g, showing a perimeter law $\mathcal{L}_{\text{min}}^{(1)} \sim \exp(-\alpha N)$, with $\alpha > 0$. Although $\mathcal{L}_{\text{min}}^{(1)} \to 0$ as $N \to \infty$ for arbitrary $g > 0$, we can still observe a drastic difference of $\mathcal{L}_{\text{min}}^{(1)}$ in the two phases (Fig. S6b), i.e., $\mathcal{L}_{\text{min}}^{(1)} \simeq 0$ in the DPP, while it has finite value in the DFP.

Loschmidt echo, rate function, and anomalous dynamical phase: Numerical results and possible signatures. Before discussing the numerical and experimental results, we briefly review several important concepts and the conclusions in previous works.

We first introduce the concept of the DPT characterized via the non-equilibrium order parameter (*7-10,24,25*). The $\mathbb{Z}_2$ global symmetry plays a key role in the DPT. In the dynamical paramagnetic phase (DPP), as $h^x > h_c^x$, the symmetry is restored, and the value of order parameter is equal to zero. In the dynamical ferromagnetic phase (DFP), as $h^x < h_c^x$, the symmetry is broken, and the order parameter has a finite value. Therefore, based

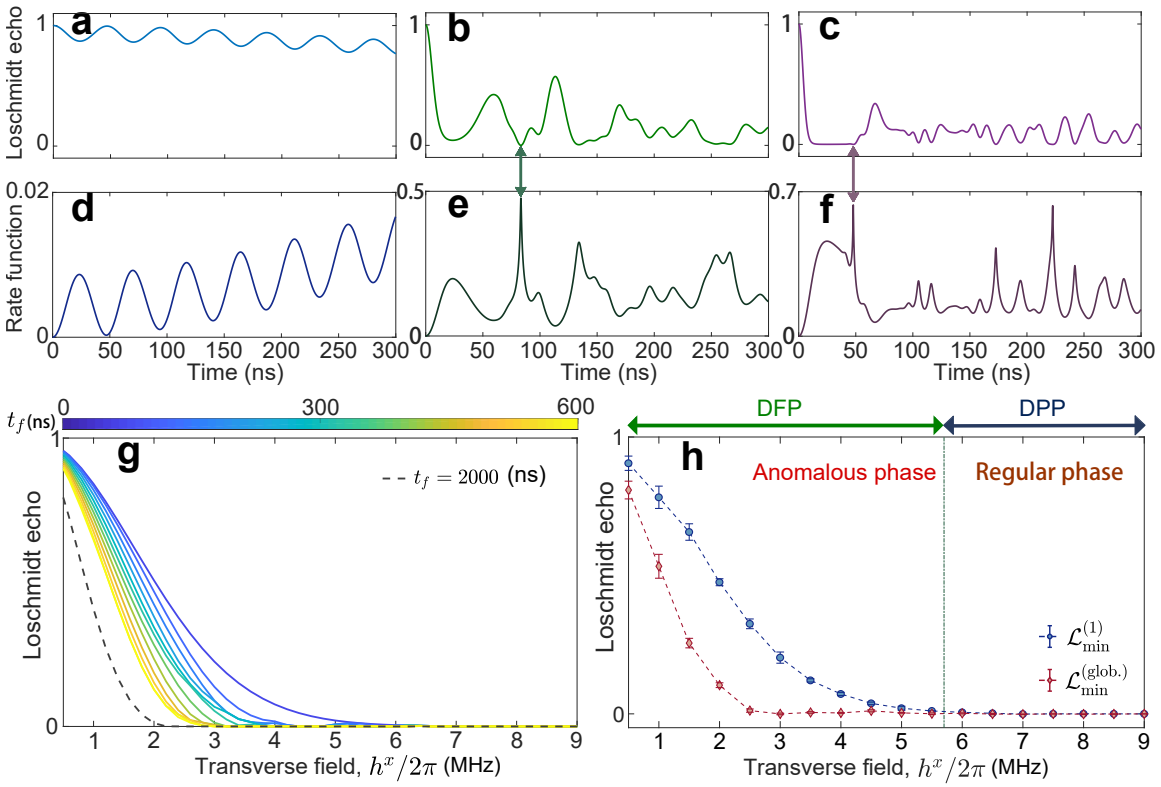

FIG. S7. **Numerical and experimental data for the long-time behaviors of the Loschmidt echo and the rate function. a,** The time evolution of the Loschmidt echo for $h^x/2\pi \simeq 1$ MHz. **b,** The time evolution of the Loschmidt echo for $h^x/2\pi \simeq 5$ MHz. **c,** The time evolution of Loschmidt echo for $h^x/2\pi \simeq 8$ MHz. **d,** The rate function of the Loschmidt echo in **a**. **e,** The rate function of the Loschmidt echo in **b**. **f,** The rate function of the Loschmidt echo in **c**. **g,** The numerically simulated value of the minimum Loschmidt echo for different finial times t_f as a function of h^x. **h,** The experimentally measured value of $\mathcal{L}_{\rm min}^{(\rm glob.)}$ as a function of h^x, with $\mathcal{L}_{\rm min}^{(\rm glob.)}$ being the minimum value of the Loschmidt echo during its time evolution with a final time of around 600 ns. The solid curves in **a**–**f** are numerical results obtained using the real parameters of the superconducting quantum simulator.

on the $\mathbb{Z}_2$ global symmetry, the non-equilibrium order parameter has a finite (zero) value in the DFP (DPP).

A different concept of DPTs is the non-equilibrium phase transition associated with the real-time dynamics of the Loschmidt echo (*7,9,11,24,25*). This is characterized by the occurrence of the non-analyticity of the rate function of the Loschmidt echo, defined as $r(t) \equiv -(1/N)\ln \mathcal{L}(t)$, during the time evolution, where the Loschmidt echo is $\mathcal{L}(t) \equiv |\langle\psi(0)|e^{iHt}|\psi(0)\rangle|^2 = |\langle\psi(0)|\psi(t)\rangle|^2$.

Then, we review the results in Refs. (*7,9,24,25*) on the relation between these two concepts of dynamical criticality, characterized via the non-equilibrium order parameter and Loschmidt echo, respectively. In Ref. (*7*), the numerical results of the Ising chain with power-law decaying interactions, characterized by a decay rate α, show that when $\alpha = 1.8$, the non-analytical point of the Loschmidt echo rate function $r(t)$ appears in the DPP, while it is absent in the DFP, merging these two concepts of dynamical criticality. In Ref. (*9*), these two concepts of dynamical criticality are studied in the LMG model, revealing that during the dynamics, the non-analyticity of the rate function occurs after (before) its first minimum point in the DFP (DPP). Different from the results in Ref. (*7*), the non-analytical cusps of the Loschmidt echo rate function in the LMG model can also be observed even though the system is in the DFP, which refers to the anomalous dynamical phase. Recently, from the perspective of Lee-Yang-Fisher zeros (*24*), the existence of the anomalous dynamical phase is also verified using an infinite matrix-product-state technique (*25*). Moreover, it has been revealed that the anomalous dynamical phase can be observed in long-range spin systems and is absent in models with short-range interactions or long-range fermionic systems (*38*).

To study the dynamical criticality characterized by the Loschmidt echo, it is essential to observe the non-analytical behavior of the rate function $r(t)$. In Fig. S7a–

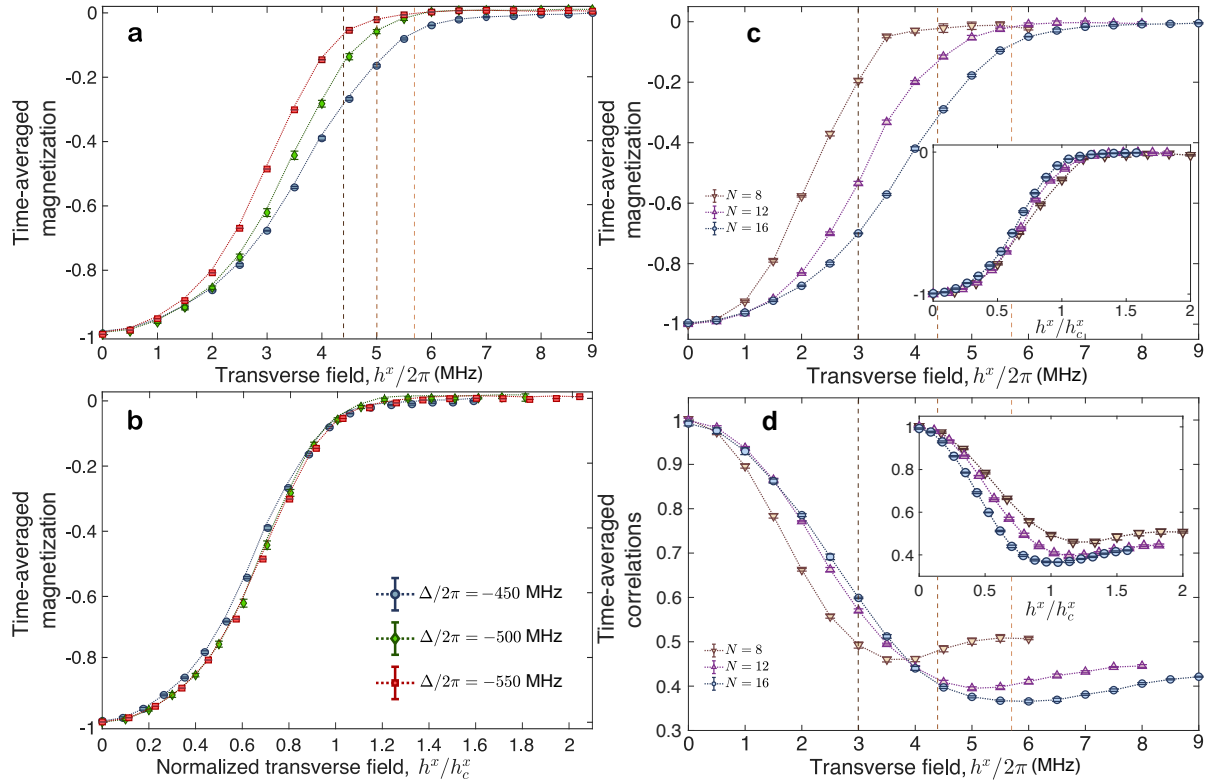

FIG. S8. **Experimental data for the quantum simulator with different values of the detuning Δ and the qubit number N. a**, The order parameter $\overline{\langle\sigma^z\rangle}$ as a function of the field strength h^x. The theoretically predicted critical points for $\Delta/2\pi \simeq -450$ MHz, -500 MHz and -550 MHz are $h_c^x/2\pi \sim 5.7$ MHz, 5.0 MHz, and 4.4 MHz, respectively, as highlighted by the dashed vertical lines. **b**, The same data in **a** but with h^x normalized by its critical value h_c^x. **c**, The order parameter $\overline{\langle\sigma^z\rangle}$ and **d**, the time-averaged correlation as a function of the field strength h^x for different qubit numbers N = 8, 12 and 16, with a detuning $\Delta/2\pi \simeq -450$ MHz. The theoretically predicted critical points for N = 8, 12 and 16 are $h_c^x/2\pi \sim 3.0$ MHz, 4.4 MHz, and 5.7 MHz, respectively, as highlighted by the dashed vertical lines. The inset figures show the same data with h^x normalized by the critical values h_c^x. The 8-qubit system consists of Q_1, Q_3, Q_6, Q_8, Q_9, Q_{11}, Q_{14}, and Q_{16} as shown in Fig. 1 of the main text. The 12-qubits system consists of Q_1, Q_2, Q_3, Q_4, Q_5, Q_6, Q_7, Q_8, Q_9, Q_{11}, Q_{14}, and Q_{16}.

f, we present the numerical results of the Loschmidt echo and the rate function with different transverse field strengths h^x. For $h^x/2\pi \simeq 1$ MHz (Fig. S7a,d) and $h^x/2\pi \simeq 5$ MHz (Fig. S7b,e), the system is in the DFP. For $h^x/2\pi \simeq 8$ MHz (Fig. S7c,f), the system is in the DPP, according to the critical point $h_c^x/2\pi \simeq 5.7$ MHz. The non-analytical point of $r(t)$ can be observed in both the DFP (Fig. S7e) and the DPP (Fig. S7f). However, in the DFP, before the first minimum point of $r(t)$, the non-analytical behavior of $r(t)$ is absent, while there is an obvious non-analyticity of $r(t)$ before its first minimum point in the DPP. As discussed in Ref. (*9*), the non-analyticities of $r(t)$ in Fig. S7e and S7f are denoted as the anomalous and regular dynamical phases, respectively.

By comparing the results in Fig. S7a–c and S7d–f, it is indicated that whether the maximum point of the rate function is non-analytical depends on how the value of Loschmidt echo at the minimum point is close to 0. Therefore, we focus on the minimum point of the Loschmidt echo. In addition, since the difference between the above-mentioned regular and anomalous dynamical phases focus on the behavior of $r(t)$ before its first minimum, we can diagnose the regular dynamical phase via the first minimum of the Loschmidt echo $\mathcal{L}_{\rm min}^{(1)}$.

As shown in Fig. S7b and S7e, although the first maximum of $r(t)$ is analytical, the non-analyticity can occur at a longer time. The corresponding behavior of the Loschmidt echo $\mathcal{L}(t)$ is that $\mathcal{L}_{\rm min}^{(1)}$ is obviously non-zero at an early time, and $\mathcal{L}(t)$ can be observed to be close to zero for a longer time. Therefore, an indirect evidence of the anomalous dynamical phase can be obtained by studying the long-time evolution of $\mathcal{L}(t)$. In Fig. S7g, we present the numerical results of the minimum $\mathcal{L}(t)$, $\mathcal{L}_{\rm min}^{\rm glob.} \equiv \min_{t\in[0,t_f]}\mathcal{L}(t)$, with t_f being the final time of

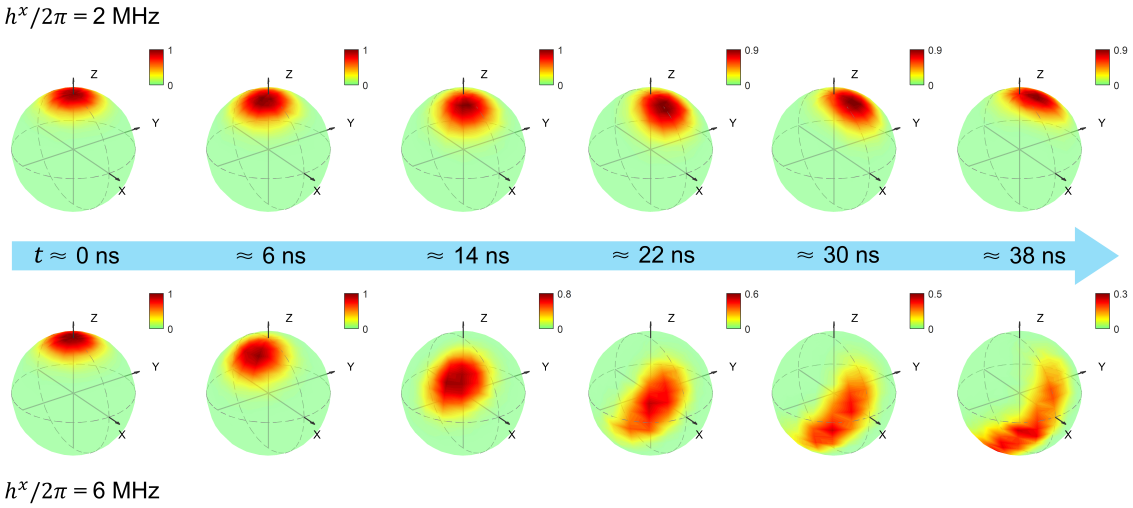

FIG. S9. **Dynamics of the quasidistribution Q-function.** The quasidistributions $Q_{\rm exp}(\theta, \phi)$ at different time intervals, for $h^x/2\pi$ =2 MHz (up) and 6 MHz (down), respectively.

the time evolution, as a function of the transverse field strength. For a given t_f, there exists a region of the transverse field strength $h^x \in [h_d^x, +\infty)$, where $\mathcal{L}_{\rm min}^{(\rm glob.)} \simeq 0$ is satisfied. With increasing t_f, the lower bound of the region h_d^x becomes smaller, indicating the occurrence of the zeros of the Loschmidt echo (the non-analyticity of the rate function) for a longer time in the DFP. In Fig. S7, we present the experimental data of the global minimum value $\mathcal{L}_{\rm min.}^{(\rm glob.)}$ with $t_f = 600$ ns, compared with the $\mathcal{L}_{\rm min}^{(1)}$. From the behavior of $\mathcal{L}_{\rm min}^{(1)}$, it is seen that the zeros of the Loschmidt echo occur in the DPP, i.e., $h^x/2\pi \in [5.7, +\infty)$ MHz, while the behavior of $\mathcal{L}_{\rm min.}^{(\rm glob.)}$ shows the occurrence of the zeros of Loschmidt in the DFP, i.e., $h^x/2\pi \in [3, +\infty)$ MHz. In addition, we numerically calculate $\mathcal{L}_{\rm min}^{(\rm glob.)}$ with $t_f = 2000$ ns, giving a broader region where the zeros of $\mathcal{L}(t)$ occurs (see Fig. S7g). It can be deduced that in the full DFP ($0 < h^x < h_c^x$), $\mathcal{L}_{\rm min}^{(\rm glob.)} \to 0$ for an infinite final time $t_f \to \infty$.

In our experiments, the time interval of the measurements is 4 ns, which is not small enough to directly observe the non-analyticity of the rate function. We employ a time interval of 1 ns for the numerical simulations in Fig. S7a-f. The observation of non-analytical points of $r(t)$ could be a further experiment, where the time resolution needs to be improved.

Additional experimental data. In Fig. S8a and S8b, we plot the experimentally measured non-equilibrium order parameter as a function of the transverse field magnitude for different values of the detuning Δ with $N = 16$ qubits. We also plot the experimentally measured non-equilibrium order parameter (Fig. S8c) and the two-site correlation (Fig. S8d) as a function of the transverse field magnitude for different qubit numbers N with a detuning $\Delta/2\pi \simeq -450$ MHz. In Fig. S9, we displayed the evolution of the experimental quasidistribution Q-function for two different transverse field magnitudes.

REFERENCES AND NOTES

1. R. P. Feynman, Simulating physics with computers. *Int. J. Theor. Phys.* **21**, 467–488 (1982).
2. I. Georgescu, S. Ashhab, F. Nori, Quantum simulation. *Rev. Mod. Phys.* **86**, 153–185 (2014).
3. J. Eisert, M. Friesdorf, C. Gogolin, Quantum many-body systems out of equilibrium. *Nat. Phys.* **11**, 124–130 (2015).
4. M. Rigol, V. Dunjko, M. Olshanii, Thermalization and its mechanism for generic isolated quantum systems. *Nature* **452**, 854–858 (2008).
5. D. A. Abanin, E. Altman, I. Bloch, M. Serbyn, *Colloquium:* Many-body localization, thermalization, and entanglement. *Rev. Mod. Phys.* **91**, 021001 (2019).
6. N. Y. Yao, A. C. Potter, I.-D. Potirniche, A. Vishwanath, Discrete time crystals: Rigidity, criticality, and realizations. *Phys. Rev. Lett.* **118**, 030401 (2016).
7. B. Žunkovič, M. Heyl, M. Knap, A. Silva, Dynamical Quantum phase transitions in spin chains with long-range interactions: Merging different concepts of nonequilibrium criticality. *Phys. Rev. Lett.* **120**, 130601 (2018).
8. A. Lerose, J. Marino, B. Žunkovič, B. Gambassi, A. Silva, Chaotic dynamical ferromagnetic phase induced by nonequilibrium quantum fluctuations. *Phys. Rev. Lett.* **120**, 130603 (2018).
9. I. Homrighausen, N. O. Abeling, V. Zauner-Stauber, J. C. Halimeh, Anomalous dynamical phase in quantum spin chains with long-range interactions. *Phys. Rev. B* **96**, 104436 (2017).
10. B. Sciolla, G. Biroli, Dynamical transitions and quantum quenches in mean-field models. *J. Stat. Mech. Theor. Exp.* P11003 (2011).
11. M. Heyl, A. Polkovnikov, S. Kehrein, Dynamical quantum phase transitions in the transverse-field Ising model. *Phys. Rev. Lett.* **110**, 135704 (2013).
12. N. Fläschner, D. Vogel, M. Tarnowski, B. S. Rem, D.-S. Lühmann, M. Heyl, J. C. Budich, L. Mathey, K. Sengstock, C. Weitenberg, Observation of dynamical vortices after quenches in a system with topology. *Nat. Phys.* **14**, 265–268 (2018).
13. H. Bernien, S. Schwartz, A. Keesling, H. Levine, A. Omran, H. Pichler, S. Choi, A. S. Zibrov, M. Endres, M. Greiner, V. Vuletić, M. D. Lukin, Probing many-body dynamics on a 51-atom quantum simulator. *Nature* **551,** 579–584 (2017).
14. J. Zhang, G. Pagano, P. W. Hess, A. Kyprianidis, P. Becker, H. Kaplan, A. V. Gorshkov, Z.-X. Gong, C. Monroe, Observation of a many-body dynamical phase transition with a 53-qubit quantum simulator. *Nature* **551**, 601–604 (2017).

15. P. Jurcevic, H. Shen, P. Hauke, C. Maier, T. Brydges, C. Hempel, B. P. Lanyon, M. Heyl, R. Blatt, C. F. Roos, Direct observation of dynamical quantum phase transitions in an interacting many-body system. *Phys. Rev. Lett.* **119**, 080501 (2017).
16. Y. Ye, Z.-Y. Ge, Y. Wu, S. Wang, M. Gong, Y.-R. Zhang, Q. Zhu, R. Yang, S. Li, F. Liang, J. Lin, Y. Xu, C. Guo, L. Sun, C. Cheng, N. Ma, Z. Y. Meng, H. Deng, H. Rong, C.-Y. Lu, C.-Z. Peng, H. Fan, X. Zhu, J.-W. Pan, Propagation and localization of collective excitations on a 24-qubit superconducting processor. *Phys. Rev. Lett.* **123**, 050502 (2019).
17. Z. Yan, Y.-R. Zhang, M. Gong, Y. Wu, Y. Zheng, S. Li, C. Wang, F. Liang, J. Lin, Y. Xu, C. Guo, L. Sun, C.-Z. Peng, K. Xia, H. Deng, H. Rong, J. Q. You, F. Nori, H. Fan, X. Zhu, J.-W. Pan, Strongly correlated quantum walks with a 12-qubit superconducting processor. *Science* **364**, 753–756 (2019).
18. P. Roushan, C. Neill, J. Tangpanitanon, V. M. Bastidas, A. Megrant, R. Barends, Y. Chen, Z. Chen, B. Chiaro, A. Dunsworth, A. Fowler, B. Foxen, M. Giustina, E. Jeffrey, J. Kelly, E. Lucero, J. Mutus, M. Neeley, C. Quintana, D. Sank, A. Vainsencher, J. Wenner, T. White, H. Neven, D. G. Angelakis, J. Martinis, Spectroscopic signatures of localization with interacting photons in superconducting qubits. *Science* **358**, 1175–1179 (2017).
19. B. Chiaro, C. Neill, A. Bohrdt, M. Filippone, F. Arute, K. Arya, R. Babbush, D. Bacon, J. Bardin, R. Barends, S. Boixo, D. Buell, B. Burkett, Y. Chen, Z. Chen, R. Collins, A. Dunsworth, E. Farhi, A. Fowler, B. Foxen, C. Gidney, M. Giustina, M. Harrigan, T. Huang, S. Isakov, E. Jeffrey, Z. Jiang, D. Kafri, K. Kechedzhi, J. Kelly, P. Klimov, A. Korotkov, F. Kostritsa, D. Landhuis, E. Lucero, J. McClean, X. Mi, A. Megrant, M. Mohseni, J. Mutus, M. McEwen, O. Naaman, M. Neeley, M. Niu, A. Petukhov, C. Quintana, N. Rubin, D. Sank, K. Satzinger, A. Vainsencher, T. White, Z. Yao, P. Yeh, A. Zalcman, V. Smelyanskiy, H. Neven, S. Gopalakrishnan, D. Abanin, M. Knap, J. Martinis, P. Roushan, Growth and preservation of entanglement in a many-body localized system. arXiv:**1910.06024** [cond-mat.dis-nn] (14 October 2019).
20. R. Ma, B. Saxberg, C. Owens, N. Leung, Y. Lu, J. Simon, D. I. Schuster, A dissipatively stabilized Mott insulator of photons, *Nature* **566**, 51–57 (2019).
21. D. I. Tsomokos, S. Ashhab, F. Nori, Fully-connected network of superconducting qubits in a cavity. *New J. Phys.* **10**, 113020 (2008).

22. H. J. Lipkin, N. Meshkov, A. J. Glick, Validity of many-body approximation methods for a solvable model: (I). Exact solutions and perturbation theory. *Nucl. Phys.* **62**, 188–198 (1965).
23. J. I. Cirac, M. Lewenstein, K. Mølmer, P. Zoller, Quantum superposition states of Bose-Einstein condensates. *Phys. Rev. A* **57**, 1208–1218 (1998).
24. V. Zauner-Stauber, J. C. Halimeh, Probing the anomalous dynamical phase in long-range quantum chains through Fisher-zero lines. *Phys. Rev. E* **96**, 062118 (2017).
25. J. C. Halimeh, V. Zauner-Stauber, Dynamical phase diagram of quantum spin chains with long-range interactions. *Phys. Rev. B* **96**, 134427 (2017).
26. M. Kitagawa, M. Ueda, Squeezed spin states. *Phys. Rev. A* **47**, 5138–5143 (1993).
27. J. Ma, X. Wang, C. P. Sun, F. Nori, Quantum spin squeezing. *Phys. Rep.* **509**, 89–165 (2011).
28. I. Frérot, T. Roscilde, Quantum critical metrology. *Phys. Rev. Lett.* **121**, 020402 (2018).
29. C. Song, K. Xu, H. Li, Y.-R. Zhang, X. Zhang, W. Liu, Q. Guo, Z. Wang, W. Ren, J. Hao, H. Feng, H. Fan, D. Zheng, D.-W. Wang, H. Wang, S.-Y. Zhu, Generation of multicomponent atomic Schrödinger cat states of up to 20 qubits. *Science* **365**, 574–577 (2019).
30. L. Pezzè, A. Smerzi, M. K. Oberthaler, R. Schmied, P. Treutlein, Quantum metrology with nonclassical states of atomic ensembles. *Rev. Mod. Phys.* **90**, 035005 (2018).
31. A. Sørensen, L.-M. Duan, J. I. Cirac, P. Zoller, Many-particle entanglement with Bose-Einstein condensates. *Nature* **409**, 63–66 (2001).
32. C. Song, K. Xu, W. Liu, C.-p. Yang, S.-B. Zheng, H. Deng, Q. Xie, K. Huang, Q. Guo, L. Zhang, P. Zhang, D. Xu, D. Zheng, X. Zhu, H. Wang, Y.-A. Chen, C.-Y. Lu, S. Han, J.-W. Pan, 10-qubit entanglement and parallel logic operations with a superconducting circuit. *Phys. Rev. Lett.* **119**, 180511 (2017).
33. K. Xu, J.-J. Chen, Y. Zeng, Y.-R. Zhang, C. Song, W. Liu, Q. Guo, P. Zhang, D. Xu, H. Deng, K. Huang, H. Wang, X. Zhu, D. Zheng, H. Fan, Emulating many-body localization with a superconducting quantum processor. *Phys. Rev. Lett.* **120**, 050507 (2018).
34. Q. Guo, C. Cheng, Z.-H. Sun, Z. Song, H. Li, Z. Wang, W. Ren, H. Dong, D. Zheng, Y.-R. Zhang, R. Mondaini, H. Fan, H. Wang, Observation of energy resolved many-body localization. arXiv:**1912.02818** [quant-ph] (5 December 2019).
35. C. Neill, P. Roushan, M. Fang, Y. Chen, M. Kolodrubetz, Z. Chen, A. Megrant, R. Barends, B. Campbell, B. Chiaro, A. Dunsworth, E. Jeffrey, J. Kelly, J. Mutus, P. J. J. O'Malley, C.

Quintana, D. Sank, A. Vainsencher, J. Wenner, T. C. White, A. Polkovnikov, J. M. Martinis, Ergodic dynamics and thermalization in an isolated quantum system. *Nat. Phys.* **12**, 1037–1041 (2016).

36. W. Lechner, P. Hauke, P. A. Zoller, Quantum annealing architecture with all-to-all connectivity from local interactions. *Sci. Adv.* **1**, e1500838 (2015).
37. B. Žunkovič, A. Silva, M. Fabrizio, Dynamical phase transitions and Loshmidt echo in the infinite-range XY model. *Phil. Trans. R. Soc. A* **374**, 20150160 (2018).
38. N. Defenu, T. Enss, J. C. Halimeh, Dynamical criticality and domain-wall coupling in long-range Hamiltonians. *Phys. Rev. B* **100**, 014434 (2019).